Available online at www.sciencedirect.com

ScienceDirect

www.elsevier.com/locate/jes

JES JOURNAL OF ENVIRONMENTAL SCIENCES

www.jesc.ac.cn

Research Article

# Nickel-based cerium zirconate inorganic complex structures for $CO_2$ valorisation via dry reforming of methane

*Juan Luis Martín-Espejo*[1], *Loukia-Pantzechroula Merkouri*[2], *Jesús Gándara-Loe*[1], *José Antonio Odriozola*[1,2], *Tomas Ramirez Reina*[1,*], *Laura Pastor-Pérez*[1,2,*]

[1] *Department of Inorganic Chemistry and Material Sciences Institute of Seville, University of Seville-CSIC, Seville 41092, Spain*

[2] *Department of Chemical and Process Engineering, University of Surrey, Guildford GU2 7XH, United Kingdom*

ARTICLE INFO

*Article history:*
Received 15 November 2022
Revised 23 December 2022
Accepted 16 January 2023
Available online 29 January 2023

*Keywords:*
$CO_2$ conversion
Dry reforming of methane
Nickel catalysts
Pyrochlore
Cerium zirconate

ABSTRACT

The increasing anthropogenic emissions of greenhouse gases (GHG) is encouraging extensive research in $CO_2$ utilisation. Dry reforming of methane (DRM) depicts a viable strategy to convert both $CO_2$ and $CH_4$ into syngas, a worthwhile chemical intermediate. Among the different active phases for DRM, the use of nickel as catalyst is economically favourable, but typically deactivates due to sintering and carbon deposition. The stabilisation of Ni at different loadings in cerium zirconate inorganic complex structures is investigated in this work as strategy to develop robust Ni-based DRM catalysts. XRD and TPR-$H_2$ analyses confirmed the existence of different phases according to the Ni loading in these materials. Besides, superficial Ni is observed as well as the existence of a $CeNiO_3$ perovskite structure. The catalytic activity was tested, proving that 10 wt.% Ni loading is the optimum which maximises conversion. This catalyst was also tested in long-term stability experiments at 600 and 800°C in order to study the potential deactivation issues at two different temperatures. At 600°C, carbon formation is the main cause of catalytic deactivation, whereas a robust stability is shown at 800°C, observing no sintering of the active phase evidencing the success of this strategy rendering a new family of economically appealing $CO_2$ and biogas mixtures upgrading catalysts.



* Corresponding authors.
*E-mails:* t.ramirezreina@surrey.ac.uk (T.R. Reina), lpperez@us.es (L. Pastor-Pérez).

https://doi.org/10.1016/j.jes.2023.01.022

## Introduction

The alarming increase of anthropogenic emissions of greenhouse gases (GHG) is encouraging extensive research to mitigate the impact of these emissions. The transition to low-carbon societies demands strategies to reduce GHG emissions, consisted mainly of $CO_2$ and $CH_4$. Most of the $CO_2$ emissions come from the consumption of fossil fuel for energy (International Energy Agency, 2018). Nevertheless, it is less known the important contribution of intensive livestock and other organic waste to GHG emissions, which come from anaerobic digestion (IPCC Fourth Assessment Report, 2014). These emissions, mainly in the form of biogas (a mixture primarily formed by $CO_2$ and $CH_4$), were regarded a waste rather than a value, but this trend is changing. Biogas industry business model is moving to two different scenarios: (i) upgrading to biomethane in order to produce biofuels to generate energy and (ii) chemical valorisation via reforming to produce syngas, primarily formed by $H_2$ and CO, which is an interesting platform chemical in chemical synthesis. Indeed, syngas is widely used as a precursor to synthetise fuels and other hydrocarbons via Fischer-Tropsch process, or other value-added products, such as methanol or acetic acid (Martín-Espejo et al., 2022). Biogas upgrading via chemical valorisation is deemed an emerging trend which may provide many opportunities to the chemical industry to tackle GHG emissions (Baena-Moreno et al., 2021). In this context, thermocatalytic biogas upgrading to syngas can be addressed via dry reforming of methane (DRM, Eq. (1)), representing an attractive way to convert $CO_2$ and $CH_4$.

$$CO_2 + CH_4 \rightarrow 2CO + 2H_2 \quad (1)$$

Typically, conventional catalysts for DRM are formed by a metal active phase which is dispersed over a support structure. Noble metals, like Ru, Rh or Pt, are reported to display great performance. Nevertheless, due their scarcity and high market prices, research focus is switching into the use of transition metals, such as Ni and Co (Jang et al., 2019; Sharifianjazi et al., 2021). Thermodynamically, DRM is a very endothermic reaction which requires high temperatures and energy inputs. At such temperatures, conventional catalysts are prone to deactivation due to sintering of the active phase and formation of coke deposits coming from side reactions such as Boudouard reaction (Eq. (2)), $CH_4$ decomposition (Eq. (3)) and CO and $CO_2$ reduction (Eqs. (4) and (5)) (Nikoo and Amin, 2011). Extensive investigation has been conducted in order to find cost-effective catalysts which avoid carbon deposition and sintering of the active phase while exhibiting acceptable catalytic performance.

$$2CO \rightarrow C + CO_2 \quad (2)$$

$$CH_4 \rightarrow C + 2H_2 \quad (3)$$

$$CO + H_2 \rightarrow C + H_2O \quad (4)$$

$$CO_2 + 2H_2 \rightarrow C + 2H_2O \quad (5)$$

Nickel-based catalysts are frequently chosen among other transition metals owing to their commendable activity, low price and availability. However, these catalysts suffer from coking and sintering, which leads to rapid deactivation. Multiple strategies have been applied to deal with the deactivation of these catalysts. Recent literature review reports highlight the most promising advances to design nickel-based DRM catalysts resistant to deactivation (Huang et al., 2022; Le saché and Reina, 2022; Yentekakis et al., 2021). The use of bimetallic formulations, the addition of promoters or the combination of different support structures are typical strategies used to enhance the performance of Ni-based catalysts, tuning the nature of the catalysts. In general, chemical and structural properties (e.g., redox, acid/base, oxygen mobility) are tuned using these strategies, making an impact on the stability and reaction mechanism. Besides, dispersion and particle size can be influenced by these parameters. As a promising alternative, the use of inorganic complex structures is aimed at stabilising the active phase in the structure while remaining active and accessible. Spinels, sandwich, tubular or mesoporous structures, hydroxyapatite, hexaaluminate, hydrotalcite, perovskites and pyrochlores have been investigated to improve the performance of DRM (Bhattar et al., 2021; Le Saché and Reina, 2022). Pyrochlores, with the formula $A_2B_2O_7$, and perovskites, $ABO_3$ and $A_2BO_4$, are mixed oxide materials in which A-site is typically substituted by a large rare-earth trivalent metal whereas B-site is substituted by a tetravalent transition metal of smaller diameter. These materials are highly crystalline, possess great thermal stability and oxygen mobility, which makes then suitable for high temperature and coke-prone processes, such as dry reforming of methane (Xu et al., 2020). For these very reasons, these mixed oxide materials have been previously studied for biogas reforming. For instance, Bhattar et al. (2020) studied the effect of the addition of Sr- and Ca- to Ni-substituted lanthanum zirconate catalysts. It was found that the addition of small amount of Sr improved the performance of the catalyst as well as an increase of the resistance of the catalyst to deactivation from carbon deposition. On the other hand, $La_2Ce_2O_7$ and $LaNiO_3$ were synthetised by Ramon et al. (2022) in order to elucidate the catalytic activity of this catalyst in DRM reaction, comparing two different synthesis methods. In another study by Ma et al. (2014), they investigated the effect of nickel-supported $La_2Zr_2O_7$ pyrochlore-like materials for steam reforming of methane, showing an excellent catalytic behaviour since coking resistance was highly improved. Two studies by Le Saché et al. (2018a, 2020) successfully proved the incorporation of Ni into a $La_2Zr_{2-x}Ni_xO_{7-\delta}$ pyrochlore structure for dry and bi-reforming of methane. According to the XRD results, the formation of a perovskite-type $La_2NiZrO_6$ is responsible for the great catalytic performance. Bai et al. (2022) have studied the effect of the substitution of nickel over both cerium and zirconium on B-site $La_2(CeZrNi)_2O_7$ for dry reforming of methane. In this study, it is believed that the exceptional oxygen vacancies and the interaction of the exsolved Ni with the support were key properties for the outstanding performance of the catalysts. Nevertheless, the incorporation of just cerium and zirconium to form a complex inorganic structure has not been tried for dry reforming despite ceriumś excellent oxygen storage/release ability (Teh et al., 2021). Attempts have been

**Table 1 – Chemical composition and physicochemical properties of the calcined catalysts.**

| Sample | $Ni_{NOM}$ (wt.%) | $Ni_{ICP}$ (wt.%) | $S_{BET}$ ($m^2/g$) | Pore volume ($\times 10^{-3}$ $cm^3/g$) |
|---|---|---|---|---|
| CZ | 0 | 0 | 4 | 9.2 |
| CZN5 | 5.0 | 5.0 | 4 | 8.8 |
| CZN10 | 10.0 | 9.5 | 3 | 7.7 |
| CZN12 | 12.5 | 11.6 | 2 | 3.0 |
| CZN15 | 15.0 | 13.7 | 2 | 1.6 |

tried for $Ce_2Zr_2O_7$ materials in photocatalysis for organic pollutants abatement, as Jayaraman and Mani (2020) have studied over a g-$C_3N_4$ support structure. $Ce_2Zr_2O_7$ has also been studied on PbS in order to study the electrochemical properties as a supercapacitor electrode (Bibi et al., 2019). As of today, no attempts have been made to study the catalytic activity of Ni-substituted $Ce_2Zr_2O_7$ for DRM.

In this scenario, this work addresses the design of inorganic complex structures to stabilise nickel, leading to robust catalysts for DRM. Under this premise, the utilisation of a thermally stable cerium zirconate oxide structure is studied, inserting and stabilising nickel within the structure ($Ce_2Zr_{2-x}Ni_xO_{7-\delta}$). This study is focused on the synthesis, catalytic activity, pre- and post-characterisation of Ni-substituted cerium zirconate for DRM. Specifically, different loading of Ni, from 0 to 15 wt.%, were incorporated to the structure, substituting on the B-site of the mixed oxide structure. Our work showcases an effective strategy to design robust and economically viable gas-phase $CO_2$ conversion catalysts with potential applications in reforming units and biogas plants.

## 1. Experimental

### 1.1. Catalyst synthesis

The catalysts were prepared through a modified version of the original Pechini method (Pechini, 1967), which is described elsewhere (Gaur et al., 2011; Kumar et al., 2016; Tietz et al., 2001). This method was chosen since it is reported to produce uniform substituted and non-susbtituted catalyst crystals (Haynes et al., 2008). Cerium nitrate ($Ce(NO_3)_3{\cdot}6H_2O$), zirconyl nitrate ($ZrO(NO_3)_2{\cdot}6H_2O$), provided by Sigma-Aldrich, and nickel nitrate ($Ni(NO_3)_2{\cdot}6H_2O$), provided by Alfa Aesar, were used as precursors. The necessary amount of each precursor was separately dissolved in deionised water and then mixed together. Citric acid (CA) was dissolved in deionised water and incorporated to the mixture of precursors while stirring at room temperature. The amount of citric acid added was molar ratio of CA:metal = 1.2:1. The solution was heated while stirring to 90°C to ensure metal complexation and ethylene glycol (EG) was added to the solution drop-wise, using a molar ratio of EG:CA = 1:1. The solution was then continuously stirred and concentrated due to evaporation of the water until the appearance of a viscous gel. The stirring was then stopped and the dense gel was left at 90-100°C to promote the polyesterification reaction between the citric acid and ethylene glycol. The decomposition of the nitrate precursors led to large plumes of $NO_x$ gas. Once the toxic gas is released, the solid was dried at 100°C overnight. The resulting compound was powdered manually in an agate mortar and then calcined in a crucible at 1000°C during 8 hr, using a heating rate of 7.5°C $min^{-1}$, to ensure phase transition. To simplify, a special notation is chosen and the catalysts will be referred as CZ, CZN5, CZN10, CZN12 and CZN15 for 0, 5, 10, 12.5 and 15 wt.% of Ni, respectively.

### 1.2. Catalyst characterisation

The textural properties of the samples were characterised by nitrogen adsorption-desorption measurements at liquid nitrogen temperature (-195.8°C) in a Micromeritics Tristar II apparatus. Before analysis, the samples were out-gassed under vacuum conditions at 250°C for 4 hr. The specific surface area ($S_{BET}$) was calculated using the Brunauer-Emmet-Teller (BET) method. The average pore volume was determined as the ratio of the pore volume and the specific surface area. This was then normalised using a coefficient which depends on the pores shape.

The metal content of Ni was measured by inductively coupled plasma spectroscopy (ICP-MS) using iCAP 7200 ICP-OES Duo (ThermoFisher Scientific) spectrometer previous microwave digestion in an ETHOS EASY (Milestone) microwave digestion platform.

X-Ray Diffraction (XRD) measurements were carried out on X'Pert Pro PANalytic diffractometer with Cu-K$\alpha$ anode at room temperature, working at a voltage of 45 kV and a current of 40 mA. The diffractograms were registered between 20 and 90° ($2\theta$) with a step size of 0.05° and a step time of 300 sec. The structural determination was done by comparison with PDF2 ICDD2000 (Powder Diffraction File 2 International Center for Diffraction Data, 2000) database.

Temperature-programmed reduction (TPR) with $H_2$ was carried out on the calcined catalysts in a conventional U-shaped quartz reactor connected with a thermal conductivity detector (TCD) using a flow of 50 mL/min of 5% $H_2$ (V/V) diluted in Ar. TPR measurements were performed using 100 mg of each catalyst and a heating rate of 10°C/min from room temperature to 900°C, using a $CO_2$ (s)/acetone cold trap to condense the water formed during the process.

Scanning electron microscopy (SEM) was carried out on the calcined catalysts under vacuum using a Hitachi S4800 SEM-FEG 0.5-30 kV voltage microscope using a cold cathode field emission gun of 1 nm resolution and equipped with a Bruker-X Flash-4010 EDS analyser.

Transmission electron microscopy (TEM) of the samples were performed on a JEOL 2100Plus (200 kV) microscope. It was equipped with an Energy Dispersive X-Ray analysis system (EDX X-Max 80T, Oxford Instruments) and a CCD camera for image recording.

### 1.3. *Catalytic behaviour*

The catalytic performance of the prepared samples for DRM reaction was evaluated under atmospheric pressure in a tubular, continuous flow fixed-bed reactor (Hastelloy reactor) with an internal diameter of 9 mm in an automatised Microactivity Reference apparatus from PID Eng&Tech. Stability tests were performed in a tubular fixed bed quartz reactor with an inside diameter of 10 mm.

The catalysts were sieved and the 100-200 μm fraction was placed in the reactor over a quartz wool bed. Prior to the activity test, the catalysts were *in situ* reduced in a flow of 50 mL/min 40% $H_2$ (V/V) in He, at 800°C for 1 hr using a heating rate of 7.5°C/min. The reaction was performed passing a reactant feed flow of 100 mL/min and molar ratio of $N_2$:$CH_4$:$CO_2$ = 2:1:1, every 50°C from 500 to 800°C until achieving the steady state on each step. The WHSV (Weight Hourly Space Velocity) was fixed at 30 L/($g_{cat}$·hr). Furthermore, stability tests were conducted at the same conditions, at 600°C and 800°C, during 100 hr.

The composition of the product gas stream was monitored using an on-line gas chromatography (Agilent Technologies) equipped with a HayeSep Q and Mol sieve 5A column. An ABB AO2020 on-line gas analyser was used to determine the composition of the product gas stream in the stability tests. The spent samples were recovered for post-reaction characterisation. In all the cases, carbon balance was closed ±5%.

The conversion ($X_i$) of the reactants (Eqs. (6) and (7)) and the $H_2$/CO molar ratio (Eq. (8)) was calculated in order to evaluate the catalytic behaviour. The conversion was calculated as follows:

$$X_{CH_4}\ (\%) = \frac{F_{CH_4,in} - F_{CH_4,out}}{F_{CH_4,in}} \cdot 100\% \quad (6)$$

$$X_{CO_2}\ (\%) = \frac{F_{CO_2,in} - F_{CO_2,out}}{F_{CO_2,in}} \cdot 100\% \quad (7)$$

$$H_2/CO = \frac{F_{H_2,out}}{F_{CO,out}} \quad (8)$$

where, *F* is the molar flow of $CH_4$, $CO_2$, $H_2$, and CO, respectively, and the subscripts in or out correspond to either the inlet and the outlet reactor flow.

## 2. Results and discussion

### 2.1. *Characterisation*

Chemical composition of nickel and textural properties of the prepared samples are listed in Table 1. The metal loading of the catalysts is close to the nominal values of 5, 10, 12.5 and 15 wt.% of Ni, witnessing the successful preparation method to carefully adjust the desired active phase loading. Still, nickel amounts of the high-Ni containing samples (CZN12 and CZN15) are slightly lower than the intended values which might indicate a threshold on optimal Ni uptake.

Regarding the textural properties of the samples, we observe the noteworthy low surface area of all of the synthesised materials in contrast to benchmark supported catalysts,

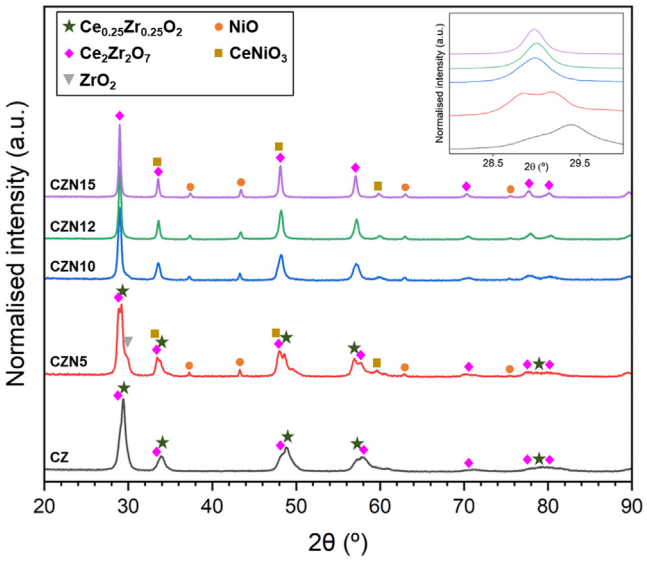


**Fig. 1 – Normalised XRD pattern of the calcined catalysts.**

which have much higher surface area (e.g., Ni-doped $Al_2O_3$-$CeO_2$ with $S_{BET}$ = 208 $m^2$/g (Marinho et al., 2021)). Therefore, this factor is important to consider since the engineered materials herein are considered to be active for DRM despite their low surface area. In other words, the DRM reaction does not necessarily require high-surface area catalysts to reach high performances as we will evidence further down in this work. Furthermore, a slight reduction of the surface area is observed when the Ni loading is increased. This reduction is more evident in the pore volume which indicates a certain degree of Ni particles blockage of the catalystsṕores.

In order to confirm the formation of the different crystalline inorganic structures, XRD analysis of the calcined catalysts was performed. The resulting normalised diffractograms of the Ni-doped cerium zirconate oxide structures with 0, 5, 10, 12.5 and 15 wt.% are presented in Fig. 1. No characteristic diffraction peaks of individual $CeO_2$ oxide phases are observed, which may suggest the incorporation of Ce into the inorganic lattice structure. CZ undoped catalyst pattern presents the characteristic diffraction features of $Ce_{0.5}Zr_{0.5}O_2$ tetragonal structure with space group P42/nmc (ICDD Card No. 00-038-1436) and $Ce_2Zr_2O_7$ pyrochlore cubic structure $Fm\bar{3}m$ (ICDD Card No. 00-008-0221). Interestingly, when Ni loading is increased, a slight shift in the diffraction peaks towards lower angles is observed between the undoped material (CZ) and the doped catalysts (CZNX). Therefore, the partial substitution of Ni on the B-site affects the crystalline structure. This shift can be observed in 29.4, 33.9, 48.9 and 58.1° 2$\theta$ of the characteristic diffraction features of $Ce_{0.5}Zr_{0.5}O_2$. The incorporation of Ni using the synthesis method produces a change in the final structure of the cerium zirconate oxide, incrementing the lattice parameter of the material, as reported when doping these structures (Haynes et al., 2008; Le Saché et al., 2018b; Pakhare et al., 2013). On the other hand, it is observed that Zr is not completely incorporated into the inorganic complex structure in CZN5 and CZN10, appearing a diffraction line around 30° 2$\theta$ which may correspond to $ZrO_2$ tetragonal structure with space group P42/nmc (ICDD Card No. 00-024-1164).

For CZN5, an interesting effect is observed. Diffraction lines abovementioned, associated to the inorganic mixed oxide, start to unfolding, distinctly observing two peaks with similar intensity instead of one, as emphasised in the inset of Fig. 1. It seems that two crystalline phases are clearly formed, appearing the characteristic features of $Ce_{0.5}Zr_{0.5}O_2$ tetragonal structure (ICDD Card No. 00-038-1436) and the separate $Ce_2Zr_2O_7$ pyrochlore cubic structure (ICDD Card No. 00-008-0221). For $Ce_2Zr_2O_7$ pyrochlore cubic structure, the diffraction lines at $2\theta$ values of 28.9, 33.6, 48.1 57.1, 59.9 and 70.4° are attributed to the (222), (400), (440), (622), (444) and (800) crystal planes. Considering the radius ratio $r_A/r_B$, which is relevant factor for $A_2B_2O_{7-\delta}$ inorganic complex structures (Bai et al., 2022; Xu et al., 2020), the substitution of Ni on B-site within the structure produces a decrease of this parameter since Ni radius is smaller than that of Zr, which is associated with a less ordered structure. When the loading of Ni is further increased, the unfolding phenomenon vanished, appearing mainly one diffraction pattern corresponding again to $Ce_2Zr_2O_7$ cubic structure (ICDD Card No. 00-008-0221). Therefore, it is proved that the incorporation of Ni produces variations in the inorganic oxides formed in this material.

Regarding the active phase, it is observed that part of the Ni is inserted in the inorganic structure. Cubic perovskite $CeNiO_3$ phase with space group $Pm\bar{3}m$ (Material project Card No. mp-866095) can be identified in all the doped materials at 33.5, 48.1 and 59.8°. Besides, the presence of some NiO domains can be observed in the diffractogram. Diffraction lines 37.3, 43.3, 62.9 and 75.4° $2\theta$ are attributed to rhombohedral NiO (ICDD Card No. 00-022-1189). In general, the intensity of the diffraction line attributed to NiO species remains the same as the Ni content increases. Interestingly, in the most intense diffraction line of NiO, it is observed a slight displacement of the peak towards higher degrees as the nickel content is increased, reaching 43.5° $2\theta$ for CZN15. This increase is associated to $NiO_{1-x}$ species, where x is higher as the increase of this diffraction line angle. Indeed, the ratio Ni/O is closer to orthorhombic $Ni_4O_3$ (mp-656887) than NiO in CZN15. This is closely related to the diffraction lines shift previously reported of the mixed oxide structure to lower angles. Therefore, it may be concluded that Ni is distributed in the lattice structure, interacting differently with the oxide species resulting of the formation of this material.

Further insights on the redox behaviour of our mixed-oxide systems were gathered by temperature-programmed reduction (TPR) experiments. The resulting $H_2$ consumption profiles are depicted in Fig. 2. The composition of the samples, interactions among the active species of the calcined catalysts and the conditions necessary for the pre-treatment step were also analysed in light of the TPR data. The undoped material CZ has been found to have small reducibility. A small $H_2$-consumption signal appears due to the possible interaction with the Ce species inserted in the catalyst. This signal appears between 400 and 540°C. Nevertheless, this reduction event is small. Overall, the observed $H_2$ consumption in the Ni-based materials is mainly due to the reducibility of Ni species upon its incorporation in the catalysts. In the profiles herein presented of the doped materials, three main reduction regions are worth considering. The first region, with a temperature peak between 365 and 375°C, can be attributed

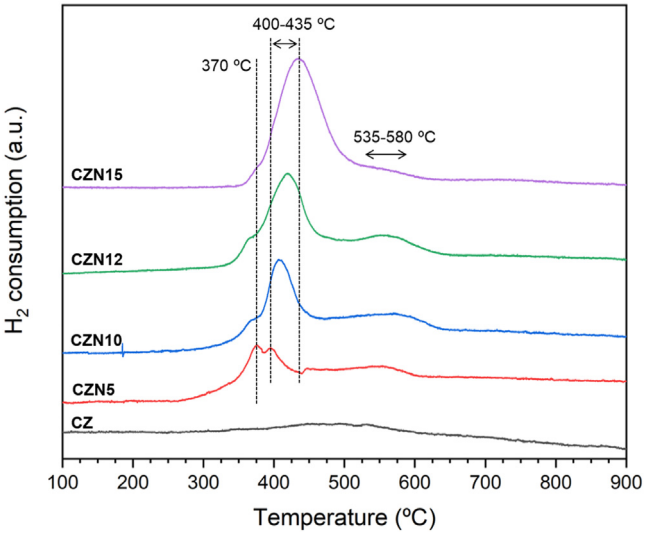


**Fig. 2 – $H_2$-TPR profile of the calcined catalysts.**

to the reduction of $NiO_{1-x}$ species which are interacting with the $Ce_{0.5}Zr_{0.5}O_2$ phase. The presence of this phase is presented mainly in CZN5 XRD in Fig. 1, which is consistent with the results. TPR signal is reduced for CZN10, CZN12 and CZN15, since this phase is disappearing when the Ni content is increased in the samples. A medium temperature region is observed between 400 and 435°C. This phase can be attributed to the interaction of $NiO_{1-x}$ species with the $Ce_2Zr_2O_7$ pyrochlore phase. In this case, it is observed that the peak is displaced to higher temperatures as the Ni content is increased, which may indicate a stronger interaction with the phase. Besides, the intensity of the signal increases with the Ni loading, which may indicate that higher Ni loadings may lead to larger proportions of $NiO_{1-x}$. Finally, the most intense signal, between 535 and 580°C, is attributed to the partial reduction of $CeNiO_3$ phase, which is more difficult to reduce. This signal, in general, decreases as the Ni content is increased.

XRD analysis was also performed on all the samples reduced at 800°C for 1 hr. $NiO_{1-x}$ species were reduced to $Ni^0$ since the characteristic peaks of $NiO_{1-x}$ shifted to higher diffraction line angles after the $H_2$ treatment. Characteristic peaks of $Ni^0$ at 44.6 and 50.0° $2\theta$ are observed (ICDD Card No. 01-087-0712). Nevertheless, $CeNiO_3$ phase still appears, which may indicate that this phase is just partially and/or superficially reduced but bulk crystalline domains remained upon the selected pre-reduction treatment.

In order to calculate the size of Ni crystallite, Scherrer equation is used for all the samples in which Ni is incorporated, using the most intense peak, 44.6° $2\theta$. The results can be observed in Table 2. In general, there is homogeneity in the

**Table 2 – Mean crystallite size of $Ni^0$ particles.**

| | Ni crystallite size (nm) |
|---|---|
| CZN5 | 32.8 |
| CZN10 | 33.7 |
| CZN12 | 31.7 |
| CZN15 | 31.1 |

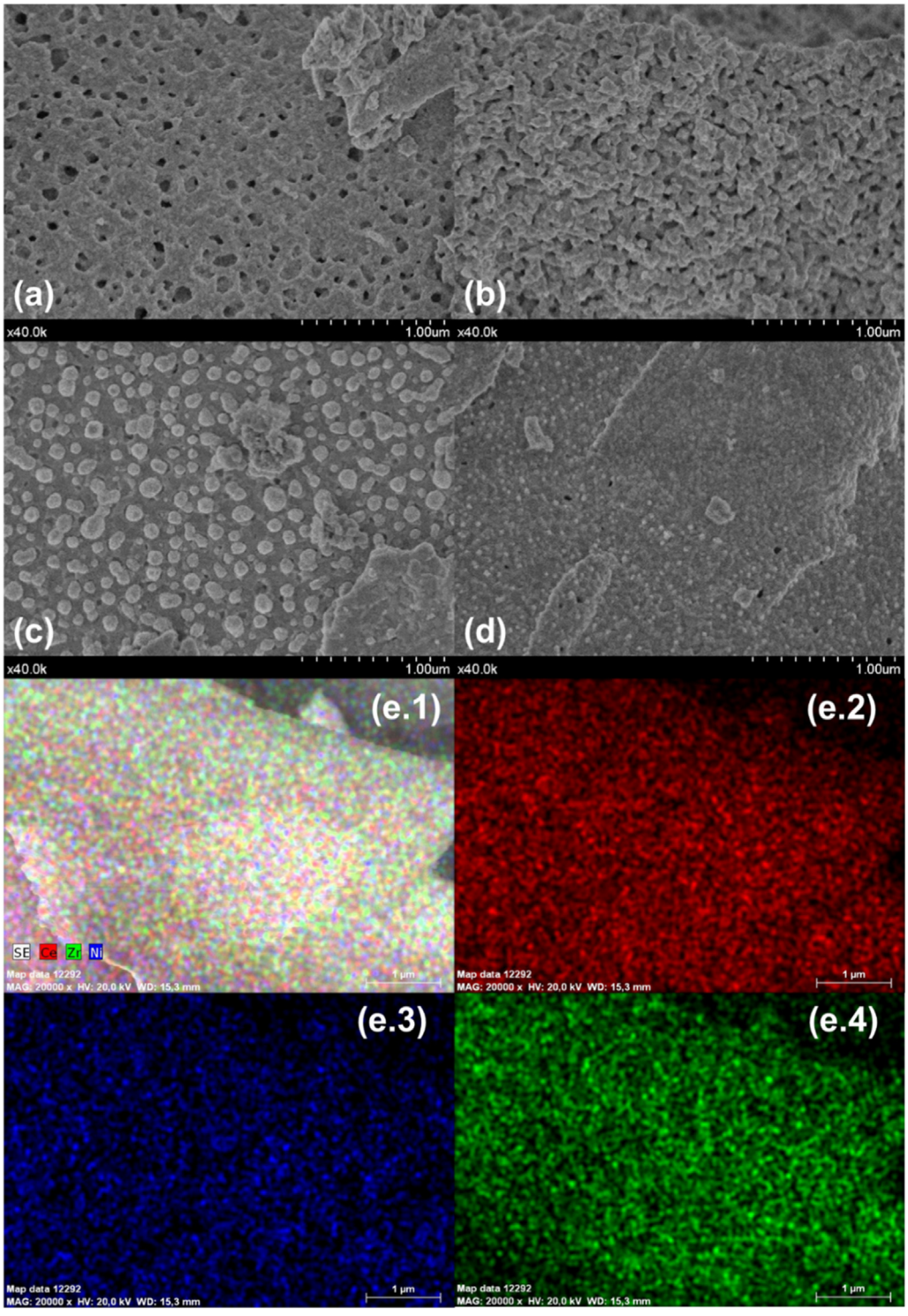


**Fig. 3 – SEM images of the reduced catalysts. (a) CZ, (b) and (c) CZN5, (d) CZN10, (e) EDX with element distribution of CZN10.**

size of Ni crystallite. No increments are observed as the Ni load is increased in the catalysts. Ni particle size is expected to be no bigger than 35 nm and well-dispersed on the surface of the inorganic structure despite the low surface area of these catalysts.

To visualise the morphology of the catalysts, SEM analysis was performed in the reduced catalysts. As can be observed in Fig. 3a, corresponding to the undoped inorganic structure CZ, a homogeneous, dense structure with small cavities is observed throughout the sample. No granular or spherical shape is observed. CZN5, on the other hand, presents two different structures. In Fig. 3b, a similar porous structure is observed, which may correspond to the $Ce_{0.5}Zr_{0.5}O_2$ phase, whereas Fig. 3c structure revealed spherical shape of $Ce_2Zr_2O_7$, as reported

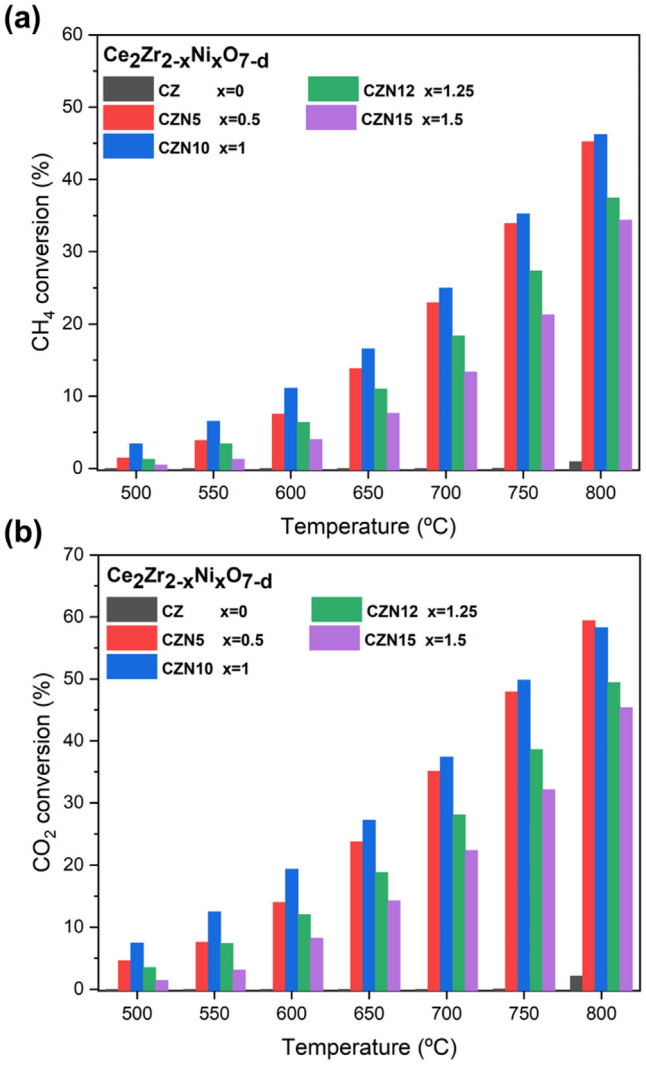


**Fig. 4 – Effect of the temperature on (a) $CH_4$ conversion and (b) $CO_2$ conversion, for all the catalysts from 500-800°C. Reaction conditions: P = 1 atm, $N_2$:$CH_4$:$CO_2$ = 2:1:1, 100 mL/min, WHSV = 30 L/(g•hr).**

elsewhere (Bibi et al., 2019). Fig. 3d corresponds to CZN10, which still present zones with some spherical shape and other complex structures. Fig. 3e presents element mapping distribution from EDX, showcasing the homogenous distribution of our active phases.

### 2.2. *Catalytic behaviour*

The reduced catalysts were tested under the above DRM reaction conditions. The effect of the temperature in DRM was studied at a temperature range from 500 to 800°C and atmospheric pressure, using a reactant gases molar ratio of $CO_2$:$CH_4$ = 1:1. As can be observed in Fig. 4, $CO_2$ conversion is greater than $CH_4$ conversion for all the catalytic systems at all temperatures. This may be due to the higher activation energy of $CH_4$ than $CO_2$ (i.e., the energy barrier to active C-H cleave bond is higher than that of $CO_2$ dissociation), requiring higher temperatures in agreement with DFT results reported elsewhere (Niu et al., 2020; Zhu et al., 2009). Besides, the possible occurrence of the reverse water-gas shift (RWGS, Eq. (9)) reaction, which competes with DRM, may contribute to the higher $CO_2$ conversion due this parallel route consuming $CO_2$ simultaneously.

$$CO_2 + H_2 \rightarrow CO + H_2O \quad (9)$$

Due to the endothermic nature of the reaction, both $CO_2$ and $CH_4$ conversion increase with temperature. At low temperatures, $CH_4$ conversion is low and far from the equilibrium values but, as the temperature rises, it gets better, reaching a conversion of 45% at 800°C for CZN10. As mentioned before, $CH_4$ needs higher temperatures to overcome the energy barrier necessary for its activation. Like $CH_4$, $CO_2$ conversion is lower at low temperature range, but it becomes higher as the temperature increases. At 800°C, the conversion reached a value of 60% for CZN10, which is closer to equilibrium conditions. These commendable catalytic results are achieved despite of the low specific surface area reported. Focusing on the two best results, CZN5 and CZN10, the conversion gap between them become closer as the temperature is increased for both $CH_4$ and $CO_2$, even surpassing $CO_2$ conversion offered by CZN10 catalysts if compared to CZN5 at 800°C.

The un-doped CZ catalyst does not show activity in DRM, as can be predicted due to the lack of active metallic Ni phase in the solid. As the metal loading is increased to 10 wt.%, the conversion of both $CH_4$ and $CO_2$ rises due to the higher Ni concentration presented in the sample. Interestingly, CZN5 presents conversion values close but lower to CZN10 despite having half of Ni metal content. This can be related to the accessibility of Ni active sites to the reactant gases due to the interaction with the phases presented in the catalyst. The presence mixed phases in CZN5 leads to remarkable activity results which are close to the those exhibited by the CZN10, which contains twice the Ni content. Particularly, this might be related to the presence of $Ce_{0.5}Zr_{0.5}O_2$ phase, which interacts more closely with Ni active centres, offering a more active catalyst according to TPR results. In any case, CZN10 shows the highest catalytic performance among the studied series. When the metal loading is further increased to 15 wt.% of Ni, a decrement of the conversion can be observed despite having more Ni in the samples. This can be related again to the accessibility of Ni active centres. The lower presence of $Ce_{0.5}Zr_{0.5}O_2$ phase as the Ni content is increased might be responsible for the decrease of conversion when compared to CZN5 and CZN10. Indeed, it appears to be an optimum amount of Ni which maximise the conversion in DRM, being close to 10 wt.%. Despite the more insertion of Ni in the structure on B-site, substituting Zr, the activity did not improve.

In terms of $H_2$/CO molar ratio, the tendency is to increase the ratio as the temperature increases, as observed in Fig. 5. This increment might be related to a higher $CH_4$ conversion, leading to better $H_2$ production and thus higher ratio. The tendency for all the doped samples is similar, which may indicate the presence of parallel competing reactions. RWGS leads to the opposite effect in the ratio since it consumes $H_2$, whereas methane decomposition generates $H_2$. In fact, among the parallel reactions affecting DRM, RWGS and $CH_4$ decom-

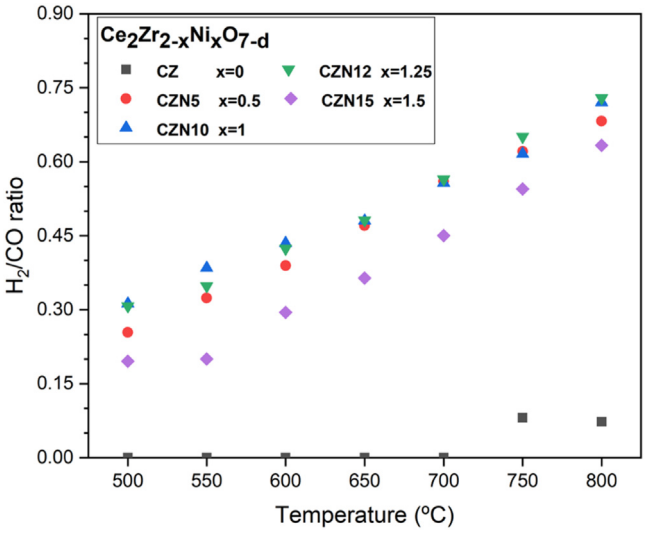


**Fig. 5 – Effect of the temperature on $H_2$/CO molar ratio, for all the catalysts from 500-800°C. Reaction conditions: P = 1 atm, $N_2$:$CH_4$:$CO_2$ = 2:1:1, WHSV = 30 L/(g•hr).**

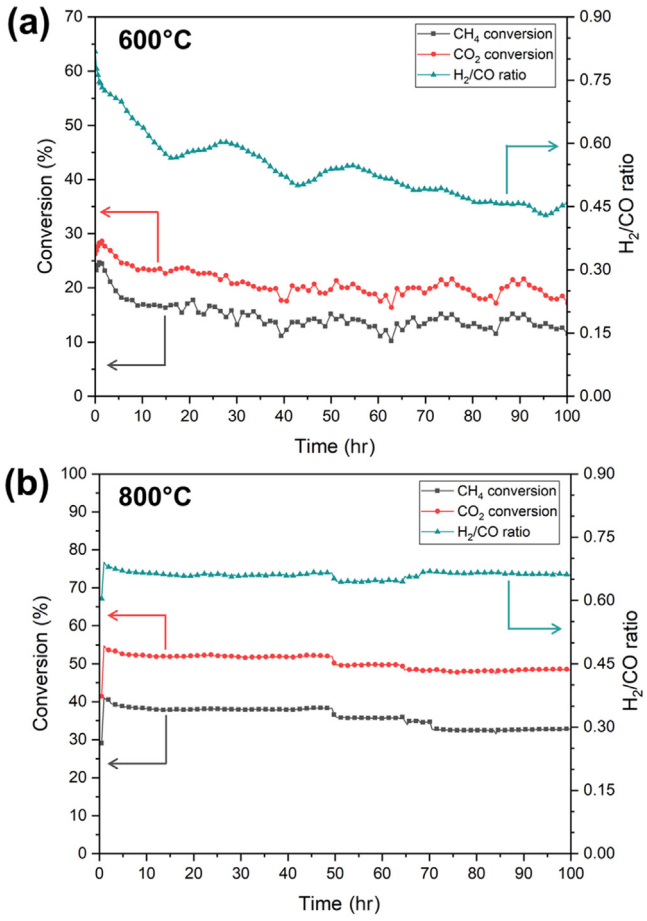


**Fig. 6 – Stability test on CZN10 over 100 hr at (a) 600°C and (b) 800°C. Reaction conditions: P = 1 atm, $N_2$:$CH_4$:$CO_2$ = 2:1:1, WHSV = 30 L/(g•hr).**

position have a remarkable influence in the reactant conversion and $H_2$/CO molar ratio, as previously reported in literature (Bradford and Vannice, 1999; Le Saché et al., 2018a, 2018b). These results may suggest that the contribution of $CH_4$ decomposition side reaction is favoured at higher temperature, thus yielding a higher $H_2$/CO ratio.

In order to further explore the catalytic performance, stability tests were performed to study how efficient the catalyst is over long-term reaction run. CZN10 was chosen to conduct the stability tests to check its behaviour over a period of 100 hr at 600°C and 800°C. The results at 600°C can be observed in Fig. 6a. This catalyst displays good stability over time. It is observed a first period of stabilisation to reach the steady state and, after that, it shows signs of small deactivation starting with conversions of $CO_2$ and $CH_4$ of 24% and 18% and achieving conversions of 18% and 12% after 100 hr on-stream, respectively. Again, the conversion of $CO_2$ is slightly larger than that of $CH_4$. Besides, a decrease in the molar $H_2$/CO ratio from 0.6 to 0.45 is noted. It is estimated a declination rate of 0.0758% and 0.0701% $hr^{-1}$ for $CH_4$ and $CO_2$, respectively. $CH_4$ is acknowledged to be activated by Ni active centres whereas $CO_2$ by the support. Therefore, it is reasonable that, if deactivation is occurring due to coke deposition or sintering of the active sites, $CH_4$ is reported to be slightly more sensitive to deactivation than $CO_2$.

At 800°C (Fig. 6b), results are slightly different and very promising. The conversion displays stable conversion levels over time. $CO_2$ conversions sets around 49%-51% whereas $CH_4$ conversion is slightly lower. $CH_4$ conversion is again reported to be more sensitive to a small deactivation than $CO_2$ conversion. The molar $H_2$/CO ratio is, in this case, quite stable and over 0.66 which be a useful syngas for some industrial applications such as hydroformylation reactions (Le Saché and Reina, 2022).

For a broad picture to place our catalysts within the DRM scenario, Table 3 offers a comparison of our results with relevant studies available in literature. Herein, we must emphasise the low surface area of the catalysts presented in this work when compared reference catalysts. Very interestingly our work demonstrates that the DRM reaction does not necessarily require high-surface area catalysts to reach high performances. In other words, the DRM reaction is not a surface-area sensitive process. In addition, we shall remark that reaction time herein reported for our stability tests is considerably higher than standard experimental data from literature, providing stronger evidence of the stability and resistance of the materials. Actually, most of the reports included in the table test the catalysts for very short time to be considered realistic stability tests and we want to draw the readers attentions to this matter since long-term stability test of 100 hr and beyond are needed as solid proof-of-concept for the catalystś resistance towards deactivation in a process like DRM.

Overall, our CZN10 is deemed as a fairly stable catalyst when tested at 800°C delivering noticeable levels of conversion and a commendable $H_2$/CO molar ratio in continuous operation during 100 hr. As a result, our best formulation leads to a valuable syngas composition with potential interest for the chemical industry. Furthermore, it is interesting to remark that operational troubles with catalystś stability observed at

**Table 3 – Comparison table of some Ni-based catalysts in literature for DRM.**

| Catalyst | $S_{BET}$ ($g/m^2$) | Temp. (°C) | WHSV (L/(g·hr)) | t (hr) | $X_{CO2}$ | $X_{CH4}$ | $H_2/CO$ ratio | Refs. |
|---|---|---|---|---|---|---|---|---|
| 8%Ni-La/$SiO_2$ | 138 | 750 | 48 | 10 | 66% | 58% | 0.8 | Li et al. (2021b) |
| 8%Ni-Ce/$SiO_2$ | 177 | 750 | 48 | 10 | 67% | 60% | 0.8 | |
| 8%Ni/$SiO_2$ | 178 | 750 | 48 | 10 | 60% | 52% | 0.8 | |
| 5%Ni/HAP-80 | 25 | 750 | 24 | 12 | 56% | 47% | 0.7 | Li et al. (2020) |
| 5%Ni/HAP-120 | 24 | 750 | 24 | 12 | 55% | 46% | 0.7 | |
| 4%Ni-MWW | 500 | 700 | 30 | 12 | 76% | 65% | 0.9 | Kweon et al. (2022) |
| 7%Ni-BEA | 481 | 700 | 30 | 12 | 78% | 76% | 0.9 | |
| 5Ni-2Ce/$SiO_2$ | 59 | 750 | 24 | 24 | 80% | 76% | 1.0 | Li et al. (2021a) |
| 5Ni-3Ce/$SiO_2$ | 49 | 750 | 24 | 24 | 81% | 78% | 0.9 | |
| 8Ni8Mo/MgO-$Al_2O_3$ | 106 | 800 | 0.98[1] | 24 | 93% | 92% | 0.9 | Abdel Karim Aramouni et al. (2021) |
| $Ni_2P/Al_2O_3$ | 161 | 700 | 30 | 10 | 81% | 75% | 1.0 | González-Castaño et al. (2021) |
| 12Ni10Nd/MgAlO | 46 | 750 | 48 | 14 | 63% | 52% | 0.8 | Yuan et al. (2022) |
| $Ce_2NiZrO_7$ (CZN10) | 2 | 800 | 30 | 100 | 50% | 38% | 0.7 | This work |

[1] w/F ($kg_{cat}$·sec/mol).

600°C can easily be overcome by rising the reaction temperature to 800°C. This is still a low temperature regime when it comes to industrial reformers which typically run on the 900-1000°C range, opening further opportunities for our catalytic formulation. Additionally, we shall highlight that the excellent catalytic performance displayed by our samples is achieved at high space velocities (i.e., 30 L/(g·hr)). Again, industrial reformers are operated at significantly lower space velocities which means that the implementation of our catalysts in a potential realistic application could lead to considerable reduction of the reforming reactor volume; or in other words, significant CAPEX savings.

### 2.3. *Post-reaction characterisation*

Deactivation of the catalyst is mainly caused by carbon deposition and/or sintering of the active phase. In order to elucidate this, the best performing catalyst was analysed after reaction by XRD in order to detect any structural changes after the different treatments it underwent. In Fig. 7, the XRD pattern of CZN10 calcined, after the reduction treatment, after DRM reaction conditions at 600°C and 800°C for 100 hr are shown. As it can be observed, the inorganic crystalline structure of the sample remains intact since there are no differences in the diffraction characteristics between the calcined and the post-reaction catalysts. This demonstrates the high thermal stability of the catalyst despite the reaction conditions. In addition, it can be observed a slight displacement of the characteristic peaks 44.4 and 51.7° 2$\theta$, corresponding to the characteristic planes of (111) and (200) of metallic $Ni^0$ to lower angles after 100 hr at 600°C, indicating that part of the surface $Ni^0$ is oxidising again to form $NiO_{1-x}$ species. On the other hand, the XRD pattern after 100 hr at 800°C shows that NiO is appearing very likely due surface oxidation when transferring the sample from the reactor to the XRD chamber.

Small growth of Ni particles is observed after reaction conditions. It was estimated a growth of the particle size from 33.7 to 39.8 and 37.3 nm at 600°C and 800°C, respectively. This small change occurred after 100 hr of reaction, which affirmed the stability and robustness of the catalyst after the substitution of Ni on the complex oxide structure, preventing partially

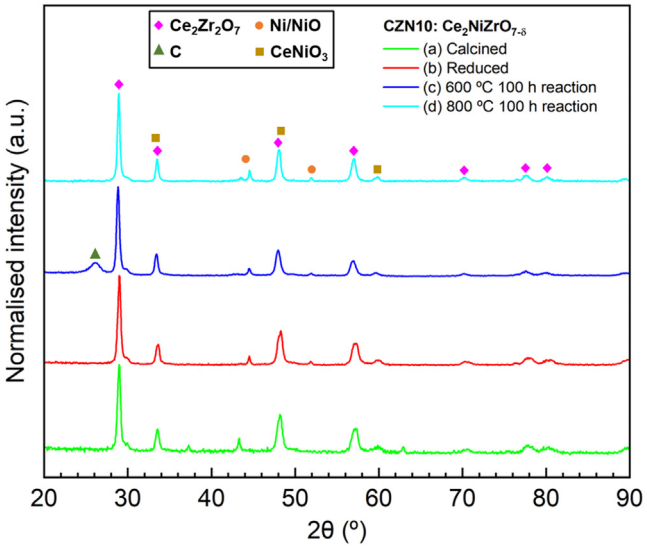


**Fig. 7 – Normalised XRD pattern of CZN10. (a) calcined, (b) reduced, (c) after 100 hr reaction at 600°C, and (d) after 100 hr reaction at 800°C.**

the sintering of the particles. It is thus estimated that a small proportion of the Ni inserted within the inorganic structure is exsolved, producing this increase in the particle size. Exsolution is actually considered a smart strategy to design efficient catalysts for energy applications when the metal has a good capacity to exsolve under reaction environments (Carrillo and Serra, 2021; Kousi et al., 2021; Kwon et al., 2017; Zhang et al., 2020).

Carbon deposition is also studied as deactivation cause. The formation of carbon is observed in XRD pattern after 100 hr at 600°C, where a peak attributed to graphitic carbon is detected. This peak corresponds to the graphite lattice plane (002) of carbon nanotubes at 26° 2$\theta$. At 800°C, no carbon structures are observed. Carbon formation is hard to avoid due to the intricate reaction, since C-H activation of $CH_4$ involves the formation of carbon species, widely studied elsewhere (Guharoy et al., 2019). Besides, the reaction tempera-

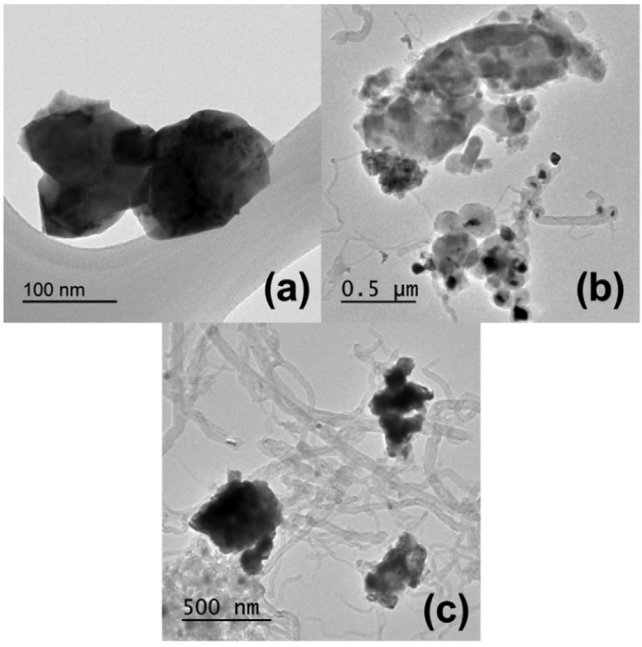


**Fig. 8 – TEM images of CZN10. (a) Reduced, (b) after 48 hr reaction and (c) after 100 hr reaction at 600°C.**

ture has an important influence on carbon deposition. It must be emphasised that carbon deposition is thermodynamically more favoured at lower temperatures, between 600 and 750°C (Nikoo and Amin, 2011). Besides, carbon deposition is closely related to Ni particle size, since the larger the clusters the more favoured the carbon deposition is. This may be another reason of carbon deposition due to the increment of Ni crystallite size.

TEM images of CZN10 of (a) reduced, (b) after 48 hr reaction and (c) after 100 hr at 600°C reaction are shown in Fig. 8. Fig. 8a shows a particle of the reduced catalyst. After 48 hr at 600°C, some carbon nanotubes (CNT) are formed, as observed in Fig. 8b. Nevertheless, the amount is negligible. After 100 hr at 600°C, significant amount of CNTs appear. These CNTs start growing from the interface of the active metal phase and the support structure, "pulling out" part of the Ni particle from the surface. Nevertheless, despite the formation of carbon deposits, the catalyst remains acceptable since this carbon is partially covering the active sites of Ni, being the rest of the Ni atoms accessible for the reaction. A similar behaviour was reported for a Ni-substitute La pyrochlore (Le Saché et al., 2018a). The main causes of catalyst deactivation at 600°C are the carbon deposits around Ni particles and the increase of Ni clusters. This situation is overcome when the reaction is run at 800°C where our post-stability XRD pattern shows a carbon-free sample which is explain the excellent conversion levels at this reaction conditions for a continuous 100 hr test.

## 3. Conclusions and perspectives

This work addresses the preparation, characterisation and testing of a series of Ni-promoted cerium zirconate oxide structures for gas-phase $CO_2$ valorisation via DRM. Structural analysis revealed the presence of different inorganic mixed oxide structures depending on the amount of nickel incorporated. Nickel is believed to be incorporated within the lattice structure, remaining part of the nickel in the surface interacting with the support structure resulting in a complex structure with different types of Ni active species as evidenced by XRD and TPR experiments.

CZN10 showed the best catalytic performance for DRM. Nevertheless, CZN5, having half of the nickel content, presented commendable conversion values, indicating that the crystalline $Ce_{0.25}Zr_{0.25}O_2$ phase, which is only presented in CZN5, is a relevant specie that makes Ni more accessible enhancing the DRM behaviour. Stability test of CZN10 over 100 hr demonstrated the long-term thermal stability of the catalysts, showing small deactivation in the low-temperature range (600°C) and excellent stability at 800°C. Such deactivation at 600°C is ascribed to graphitic carbon deposition as evidenced by TEM. XRD analysis after 100 hr hours revealed that the crystalline structure of the catalyst remained intact and part of the nickel was exsolved, slightly increasing the particle size of the Ni clusters, which are responsible for the activity of the catalyst. Potential regeneration of spent catalyst in the low-temperature operation range (600°C) should be further investigated as smart strategy to reuse the catalysts in realistic applications.

All in all, this work showcases a strategy to design thermally stable catalysts based on nickel promoted cerium-zirconium mixed oxides where nickel is incorporated within the structure, being able to withstand DRM conditions and deliver high quality syngas for long-term operations. Very importantly, the remarkable performance herein demonstrated by this Ni-engineered catalysts is achieved at relatively high space velocities when compared to industrial reformers which means that they can be instrumental for CAPEX savings in realistic applications while also paving the way to design compact DRM units that might fit very well in the biogas processing industry.

## Declaration of Competing Interest

The authors declare that they have no known competing financial interests or personal relationships that could have appeared to influence the work reported in this article.

## Acknowledgements

This work was supported by grant PID2019-108502RJ-I00 and grant IJC2019-040560-I both funded by MCIN/AEI/10.13039/501100011033 as well as RYC2018-024387-I funded by MCIN/AEI/10.13039/501100011033 and by ESF Investing in your future.

## References

Abdel Karim Aramouni, N., Zeaiter, J., Kwapinski, W., J Leahy, J., Ahmad, M.N., 2021. Molybdenum and nickel-molybdenum nitride catalysts supported on MgO-$Al_2O_3$ for the dry

reforming of methane. J. $CO_2$ Util. 44, 101411. doi:10.1016/j.jcou.2020.101411.
Baena-Moreno, F.M., Le Saché, E., Hurd Price, C.A., Reina, T.R., Navarrete, B., 2021. From biogas upgrading to $CO_2$ utilization and waste recycling: a novel circular economy approach. J. $CO_2$ Util. 47, 101496. doi:10.1016/j.jcou.2021.101496.
Bai, J., Fu, Y., Kong, W., Pan, B., Yuan, C., Li, S., et al., 2022. Design of Ni-substituted $La_2(CeZrNi)_2O_7$ pyrochlore catalysts for methane dry reforming. ChemNanoMat 8. doi:10.1002/cnma.202100422.
Bhattar, S., Abedin, M.A., Kanitkar, S., Spivey, J.J., 2021. A review on dry reforming of methane over perovskite derived catalysts. Catal. Today 365, 2–23. doi:10.1016/j.cattod.2020.10.041.
Bhattar, S., Abedin, M.A., Shekhawat, D., Haynes, D.J., Spivey, J.J., 2020. The effect of La substitution by Sr- and Ca- in Ni substituted Lanthanum Zirconate pyrochlore catalysts for dry reforming of methane. Appl. Catal. A Gen. 602, 117721. doi:10.1016/j.apcata.2020.117721.
Bibi, N., Xia, Y., Ahmad, I., Shabbir, S., Ahmed, S., Zhu, Y., et al., 2019. Mesoporous $Ce_2Zr_2O_7$/PbS nanocomposite with an excellent supercapacitor electrode performance and cyclic stability. ChemistrySelect 4, 655–661. doi:10.1002/slct.201803503.
Bradford, M.C.J., Vannice, M.A., 1999. $CO_2$ reforming of $CH_4$. Catal. Rev. 41, 1–42. doi:10.1081/CR-100101948.
Carrillo, A.J., Serra, J.M., 2021. Exploring the stability of Fe–Ni alloy nanoparticles exsolved from double-layered perovskites for dry reforming of methane. Catalysts 11, 741. doi:10.3390/catal11060741.
Gaur, S., Haynes, D.J., Spivey, J.J., 2011. Rh, Ni, and Ca substituted pyrochlore catalysts for dry reforming of methane. Appl. Catal. A Gen. 403, 142–151. doi:10.1016/j.apcata.2011.06.025.
González-Castaño, M., le Saché, E., Berry, C., Pastor-Pérez, L., Arellano-García, H., Wang, Q., et al., 2021. Nickel phosphide catalysts as efficient systems for $CO_2$ upgrading via dry reforming of methane. Catalysts 11, 446. doi:10.3390/catal11040446.
Guharoy, U., Ramirez Reina, T., Olsson, E., Gu, S., Cai, Q., 2019. Theoretical insights of $Ni_2P$ (0001) surface toward its potential applicability in $CO_2$ conversion via dry reforming of methane. ACS Catal. 9, 3487–3497. doi:10.1021/acscatal.8b04423.
Haynes, D., Berry, D., Sshehawat, D., Spivey, J., 2008. Catalytic partial oxidation of n-tetradecane using pyrochlores: effect of Rh and Sr substitution. Catal. Today 136, 206–213. doi:10.1016/j.cattod.2008.02.012.
Huang, L., Li, D., Tian, D., Jiang, L., Li, Z., Wang, H., et al., 2022. Optimization of Ni-based catalysts for dry reforming of methane via alloy design: a review. Energy Fuels 36, 5102–5151. doi:10.1021/acs.energyfuels.2c00523.
International Energy Agency, 2018. International Energy Agency. CO2 emissions from fuel combustion-highlights. Paris, France.
IPCC Fourth Assessment Report, 2014. Climate Change 2014: synthesis report. Contribution of Working Groups I, II and III to the Fifth Assessment Report of the Intergovernmental Panel on Climate Change. Geneva, Switzerland.
Jang, W.J., Shim, J.O., Kim, H.M., Yoo, S.Y., Roh, H.S., 2019. A review on dry reforming of methane in aspect of catalytic properties. Catal. Today 324, 15–26. doi:10.1016/j.cattod.2018.07.032.
Jayaraman, V., Mani, A., 2020. Interfacial coupling effect of high surface area Pyrochlore like $Ce_2Zr_2O_7$ over 2D g-$C_3N_4$ sheet photoactive material for efficient removal of organic pollutants. Sep. Purif. Technol. 235, 116242. doi:10.1016/j.seppur.2019.116242.
Kousi, K., Tang, C., Metcalfe, I.S., Neagu, D., 2021. Emergence and future of exsolved materials. Small 17, 2006479. doi:10.1002/smll.202006479.
Kumar, N., Wang, Z., Kanitkar, S., Spivey, J.J., 2016. Methane reforming over Ni-based pyrochlore catalyst: deactivation studies for different reactions. Appl. Petrochem. Res. 6, 201–207. doi:10.1007/s13203-016-0166-x.
Kweon, S., Kim, Y.W., Shin, C.H., Park, M.B., Min, H.K., 2022. Nickel silicate beta zeolite prepared by interzeolite transformation: a highly active and stable catalyst for dry reforming of methane. Chem. Eng. J. 431, 133364. doi:10.1016/j.cej.2021.133364.
Kwon, O., Sengodan, S., Kim, K., Kim, Gihyeon, Jeong, H.Y., Shin, J., et al., 2017. Exsolution trends and co-segregation aspects of self-grown catalyst nanoparticles in perovskites. Nat. Commun. 8, 15967. doi:10.1038/ncomms15967.
Le Saché, E., Pastor-Pérez, L., Garcilaso, V., Watson, D.J., Centeno, M.A., Odriozola, J.A., et al., 2020. Flexible syngas production using a $La_2Zr_{2-x}Ni_xO_{7-\delta}$ pyrochlore-double perovskite catalyst: towards a direct route for gas phase $CO_2$ recycling. Catal. Today 357, 583–589. doi:10.1016/j.cattod.2019.05.039.
Le Saché, E., Pastor-Pérez, L., Watson, D., Sepúlveda-Escribano, A., Reina, T.R., 2018a. Ni stabilised on inorganic complex structures: superior catalysts for chemical CO2 recycling via dry reforming of methane. Appl. Catal. B Environ. 236, 458–465. doi:10.1016/j.apcatb.2018.05.051.
Le Saché, E., Reina, T.R., 2022. Analysis of Dry Reforming as direct route for gas phase $CO_2$ conversion. The past, the present and future of catalytic DRM technologies. Prog. Energy Combust. Sci. 89, 100970. doi:10.1016/j.pecs.2021.100970.
Le Saché, E, Santos, J.., Smith, T.J., Centeno, M.A., Arellano-Garcia, H., Odriozola, J.A., Reina, T.R., 2018b. Multicomponent Ni-$CeO_2$ nanocatalysts for syngas production from $CO_2$/$CH_4$ mixtures. J. $CO_2$ Util. 25, 68–78. doi:10.1016/j.jcou.2018.03.012.
Li, Bin, Yuan, X., Li, Baitao, Wang, X., 2021a. Ceria-modified nickel supported on porous silica as highly active and stable catalyst for dry reforming of methane. Fuel 301, 121027. doi:10.1016/j.fuel.2021.121027.
Li, Bin, Yuan, X., Li, Baitao, Wang, X., 2020. Impact of pore structure on hydroxyapatite supported nickel catalysts (Ni/HAP) for dry reforming of methane. Fuel Process. Technol. 202, 106359. doi:10.1016/j.fuproc.2020.106359.
Li, Bin, Yuan, X., Li, L., Li, Baitao, Wang, X., Tomishige, K., 2021b. Lanthanide oxide modified nickel supported on mesoporous silica catalysts for dry reforming of methane. Int. J. Hydrog. Energy 46, 31608–31622. doi:10.1016/j.ijhydene.2021.07.056.
Ma, Y., Wang, X., You, X., Liu, J., Tian, J., Xu, X., et al., 2014. Nickel-supported on $La_2Sn_2O_7$ and $La_2Zr_2O_7$ pyrochlores for methane steam reforming: insight into the difference between tin and zirconium in the B site of the compound. ChemCatChem 6, 3366–3376. doi:10.1002/cctc.201402551.
Marinho, A.L.A., Toniolo, F.S., Noronha, F.B., Epron, F., Duprez, D., Bion, N., 2021. Highly active and stable Ni dispersed on mesoporous $CeO_2$-$Al_2O_3$ catalysts for production of syngas by dry reforming of methane. Appl. Catal. B Environ. 281, 119459. doi:10.1016/j.apcatb.2020.119459.
Martín-Espejo, J.L., Gandara-Loe, J., Odriozola, J.A., Reina, T.R., Pastor-Pérez, L., 2022. Sustainable routes for acetic acid production: traditional processes vs a low-carbon, biogas-based strategy. Sci. Total Environ. 840, 156663. doi:10.1016/J.SCITOTENV.2022.156663.
Nikoo, M.K., Amin, N.A.S., 2011. Thermodynamic analysis of carbon dioxide reforming of methane in view of solid carbon formation. Fuel Process. Technol. 92, 678–691. doi:10.1016/j.fuproc.2010.11.027.
Niu, J., Guo, F., Ran, J., Qi, W., Yang, Z., 2020. Methane dry ($CO_2$) reforming to syngas ($H_2$/CO) in catalytic process: from experimental study and DFT calculations. Int. J. Hydrog. Energy 45, 30267–30287. doi:10.1016/j.ijhydene.2020.08.067.
Pakhare, D., Wu, H., Narendra, S., Abdelsayed, V., Haynes, D., Shekhawat, D., et al., 2013. Characterization and activity study of the Rh-substituted pyrochlores for $CO_2$ (dry) reforming of

$CH_4$. Appl. Petrochem. Res. 3, 117–129. doi:10.1007/s13203-013-0042-x.

Pechini, M.P., 1967. Method of preparing lead and alkaline earth titanates and niobates and coating method using the same to form a capacitor. 3330697.

Ramon, A.P., Li, X., Clark, A.H., Safonova, O.V., Marcos, F.C., Assaf, E.M., et al., 2022. *In situ* study of low-temperature dry reforming of methane over $La_2Ce_2O_7$ and $LaNiO_3$ mixed oxides. Appl. Catal. B Environ. 315, 121528. doi:10.1016/j.apcatb.2022.121528.

Sharifianjazi, F., Esmaeilkhanian, A., Bazli, L., Eskandarinezhad, S., Khaksar, S., Shafiee, P., et al., 2021. A review on recent advances in dry reforming of methane over Ni- and Co-based nanocatalysts. Int. J. Hydrog. Energy doi:10.1016/j.ijhydene.2021.11.172.

Teh, L.P., Setiabudi, H.D., Timmiati, S.N., Aziz, M.A.A., Annuar, N.H.R., Ruslan, N.N., 2021. Recent progress in ceria-based catalysts for the dry reforming of methane: a review. Chem. Eng. Sci. 242, 116606. doi:10.1016/j.ces.2021.116606.

Tietz, F., Arul Raj, I., Jungen, W., Stöver, D., 2001. High-temperature superconductor materials for contact layers in solid oxide fuel cells: I. Sintering behavior and physical properties at operating temperatures. Acta Mater. 49, 803–810. doi:10.1016/S1359-6454(00)00385-2.

Xu, J., Xi, R., Xu, X., Zhang, Y., Feng, X., Fang, X., et al., 2020. $A_2B_2O_7$ pyrochlore compounds: a category of potential materials for clean energy and environment protection catalysis. J. Rare Earths 38, 840–849. doi:10.1016/j.jre.2020.01.002.

Yentekakis, I.V., Panagiotopoulou, P., Artemakis, G., 2021. A review of recent efforts to promote dry reforming of methane (DRM) to syngas production via bimetallic catalyst formulations. Appl. Catal. B Environ. 296, 120210. doi:10.1016/j.apcatb.2021.120210.

Yuan, X., Li, B., Wang, X., Li, B., 2022. Synthesis gas production by dry reforming of methane over Neodymium-modified hydrotalcite-derived nickel catalysts. Fuel Process. Technol. 227, 107104. doi:10.1016/j.fuproc.2021.107104.

Zhang, J., Gao, M.R., Luo, J.L., 2020. *In situ* exsolved metal nanoparticles: a smart approach for optimization of catalysts. Chem. Mater. 32, 5424–5441. doi:10.1021/acs.chemmater.0c00721.

Zhu, Y.A., Chen, D., Zhou, X.G., Yuan, W.K., 2009. DFT studies of dry reforming of methane on Ni catalyst. Catal. Today 148, 260–267. doi:10.1016/j.cattod.2009.08.022.